Journal of Maps

ISSN: 1744-5647 (Online) Journal homepage: www.tandfonline.com/journals/tjom20

# Geomorphology of Krieger Crater (Moon)

Claudia Collu , Marco Casu , Francesco Dessì & Maria Teresa Melis

**To cite this article:** Claudia Collu , Marco Casu , Francesco Dessì & Maria Teresa Melis (2026) Geomorphology of Krieger Crater (Moon), Journal of Maps, 22:1, 2698223, DOI: 10.1080/17445647.2026.2698223

**To link to this article:** https://doi.org/10.1080/17445647.2026.2698223

JOURNAL OF MAPS
2026, VOL. 22, NO. 1, 2698223
https://doi.org/10.1080/17445647.2026.2698223



# Geomorphology of Krieger Crater (Moon)

Claudia Collu[a,b], Marco Casu[a,b], Francesco Dessì[a] and Maria Teresa Melis [a]

[a]Department of Chemical and Geological Sciences, University of Cagliari, Monserrato, Italy; [b]Department of Civil, Constructional and Environmental Engineering, Sapienza University of Rome, Rome, Italy

**ABSTRACT**
Krieger crater is a ~25 km diameter Imbrian complex crater located in Oceanus Procellarum, within the northern Aristarchus–Harbinger region on the Moon. This work presents a new high-resolution geomorphological map derived from integrated analysis of LRO NAC imagery, SLDEM2015 topography, and Moon Mineralogy Mapper (M3) hyperspectral data. The combined photogeological, morphometric, and spectral investigation led to the identification of 20 geomorphological units grouped into Highland, Mare, and Crater-related classes. The analyses reveal that Krieger experienced a complex origin and post-impact evolution. Rim asymmetry, heterogeneous ejecta distribution, impact melt differentiation, and olivine-bearing volcanic materials indicate an oblique impact followed by significant floor uplift and internal magmatic intrusion, consistent with the evolution of floor-fractured craters. Subsequent Eratosthenian impacts further reworked the crater, excavating deeper materials and enhancing compositional heterogeneity. The resulting map provides new insights into the interplay between impact processes, tectonics, and volcanism in shaping the geological evolution of the region.

**Key policy highlights**

- A geomorphological map of Krieger crater at 1:200,000 scale identifies 20 distinct units, including Highland, Mare, and Crater-related deposits, based on combined spectral, morphometric, and photogeological criteria, providing a revised spatial representation of surface units and geological relationships within the study area.
- The map documents not only ejecta, wall, and floor units, but also key geological linear features such as wrinkle ridges and the volcanic channel of Rima Krieger, enhancing structural interpretation.
- Integrated morphological and hyperspectral mapping reveals a complex impact origin followed by floor uplift and volcanic activity, recorded in the spatial arrangement of mapped units.
- The cartographic synthesis improves understanding of floor-fractured crater evolution and supports reproducible planetary geological mapping.

**ARTICLE HISTORY**
Received 27 February 2026
Revised 23 June 2026
Accepted 25 June 2026

**KEYWORDS**
Krieger crater; lunar geomorphology; floor-fractured crater; lunar hyperspectral analysis; M3 hyperspectral data

## 1. Introduction

Impact craters represent the most prominent features of the lunar surface, exhibiting a diverse range of morphological features, reflecting variations in impactor properties (including size, velocity, and angle), target composition, and post-impact processes (Kenkmann et al., 2014). Craters can be categorized by their diameter, with simple craters smaller than 15 km in diameter, and complex craters exceeding 20 km. Krieger is a complex crater formed during the Imbrian Period (3.85–3.16 Ga) (Zisk et al., 1977) with a ~25 km diameter, located in the Oceanus Procellarum, on the western near-side of the Moon, precisely in the northern area of the Aristarchus–Harbinger Region, well known for its unique and complex geological formations (Zisk et al., 1977), as shown in Figure 1.

Krieger exhibits an uncommon configuration, characterized by a distinct polygonal shape of the crater rim, partially overlaid by the smaller Eratosthenian simple crater in the southern section, named Van Biesbroeck. Moreover, the floor of Krieger includes several unique landforms and concentric features. For this reason, it has been classified as a floor fractured crater (FFC), class III, by Jozwiak et al. (2012) . The asymmetric ejecta blanket extends in a north–south direction, overlapping the crater rim. The western rim is breached, and a rille, Rima Krieger, extends outward, showing deep, angular meanders (Podda et al., 2020) consistent with variable proportions of pyroxene and olivine (Cloutis et al., 1986; Sunshine & Pieters, 1998). Positioned southeast of Krieger are two smaller Eratosthenian craters,

**CONTACT** Claudia Collu Claudia.collu@uniroma1.it Department of Chemical and Geological Sciences, University of Cagliari, Cittadella Universitaria (Block A), S.S. 554 bivio per Sestu, 09042 Monserrato (CA), Italy

Supplemental map for this article can be accessed online at https://doi.org/10.1080/17445647.2026.2698223.

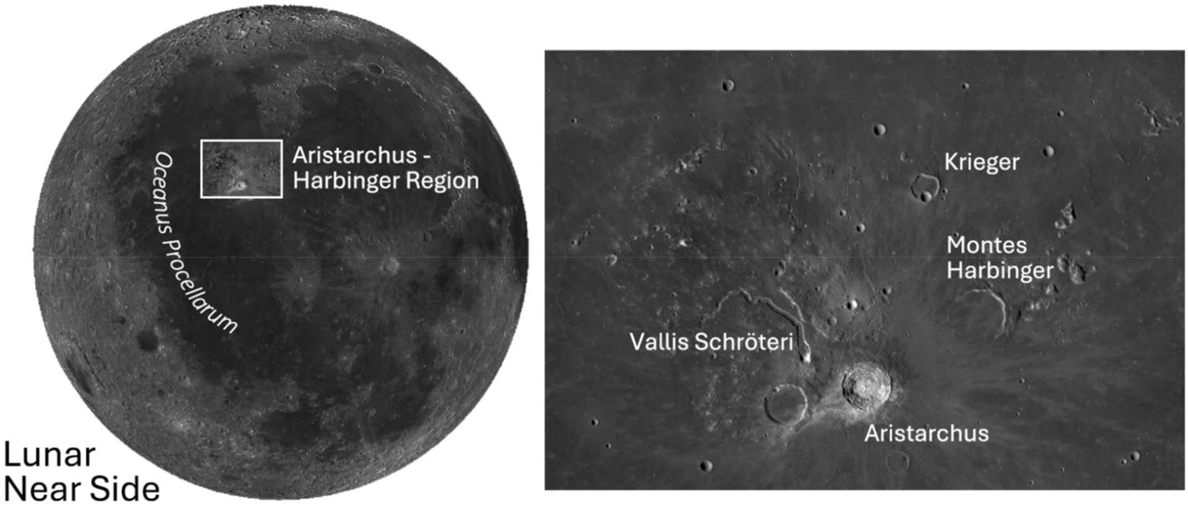


**Figure 1.** Location of Krieger crater in the Aristarchus–Harbinger Region (Oceanus Procellarum), one of the most geologically diverse areas of comparable size on the Moon, characterized by mare basalts of various ages, sinuous rilles, including the largest, Vallis Schröteri, volcanic features, and pre-mare highland massifs (Zisk et al., 1977). Montes Harbinger are interpreted as remnants of the most conspicuous raised ring of the Imbrium basin, forming isolated massifs surrounded by mare deposits of Oceanus Procellarum. Krieger crater is located in the northern part of the region, at the boundary between mare basalts and pre-Imbrian highland material.

Rocco and Ruth. Additionally, Krieger is surrounded by numerous wrinkle ridges trending from north-northeast to south-southwest (Collu et al., 2021).

In this work, a geomorphological mapping of Krieger crater is presented (see the Main Map), based on the integrated use of high-resolution NAC imagery, SLDEM2015 topography, and M3 hyperspectral data (Chandrayaan-1 mission), as described in Collu et al. (2021). This multi-source dataset allows for a consistent and spatially constrained interpretation of surface morphology and composition, leading to a detailed classification of geomorphological units and a refined reconstruction of the crater's evolutionary history. The approach emphasizes the synergy between morphological and spectral information, with the aim of improving the interpretative framework of complex lunar crater environments.

## 2. Methodology

The investigation of the Krieger crater region is based on an integrated multi-source remote sensing approach combining photogeological, morphometric, and spectral analyses. High-resolution NAC images (0.5 m/pixel) were used for detailed photogeological mapping and surface feature identification, while SLDEM2015 digital elevation data were used for topographic analysis (Figure 2).

Surface compositional analysis was performed using M3 hyperspectral reflectance data. Given the old and heavily modified nature of Krieger crater, where primary morphological features are significantly overprinted by subsequent impact and volcanic processes, compositional information is essential to support the discrimination of geomorphological units that may exhibit similar morphological expression but different geological origins.

A summary of all datasets and processing steps is provided in Table 1.

Given the geological setting of the study area (Zisk et al., 1977), the surface materials within the Krieger crater region are expected to include mafic mare basalts dominated by pyroxene-bearing compositions, as well as older pre-mare highland-related materials characterized by higher reflectance and weaker or absent mafic absorptions. To perform a first-order spectral characterization of these compositional contrasts, a false-color composite image was generated from M3 data, assigning the 1 μm integrated band depth to the red channel, the 2 μm integrated band depth to the green channel, and the reflectance at 1.58 μm to the blue channel. The 1 and 2 μm band depths highlight the presence and relative abundance of mafic minerals, primarily pyroxenes, which exhibit diagnostic absorption features at these wavelengths (Adams, 1974; Cloutis & Gaffey, 1991; Klima et al., 2007), while the reflectance at 1.58 μm, located between the two main mafic absorption bands where pyroxene absorptions are minimal, serves as a proxy for overall surface brightness. Materials with higher reflectance and weaker mafic signatures, potentially including highland-related components, appear brighter in this channel, allowing their distinction from darker, mafic-rich mare surfaces. This composite thus provides an immediate visual assessment of the spatial distribution of compositional endmembers within the study area and was used to guide the selection of representative regions of interest for endmember extraction.

Compositional units were mapped using the Spectral Angle Mapper (SAM) algorithm (Kruse et al., 1993)

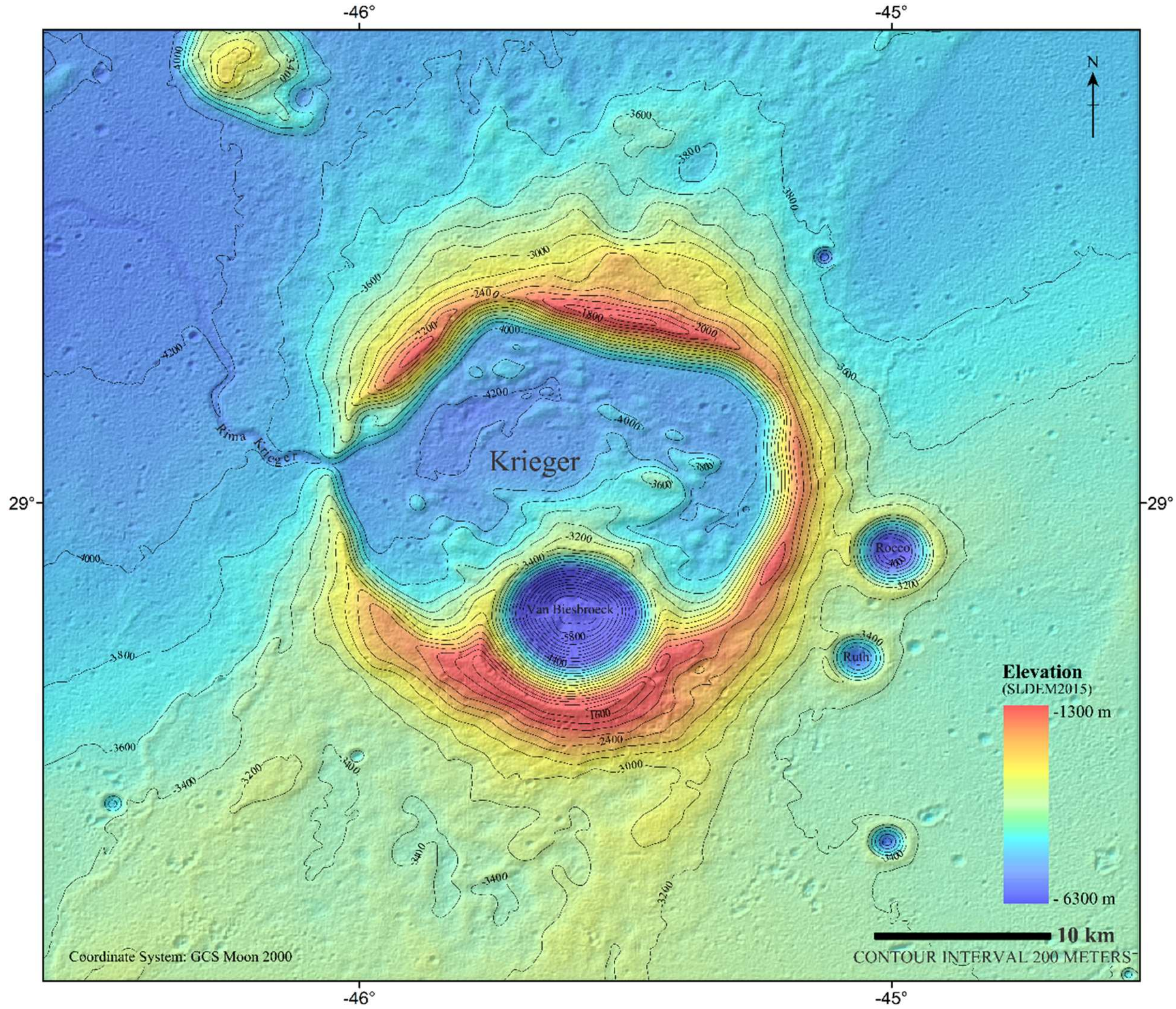


**Figure 2.** Topographic map of Kriger crater region. Heights range between −6321 and −1328 meters, with a general slope trending toward north-west. Rim-to-rim diameter is ∼ 25,2 km, with a rim height significantly dissimilar from eastern part (∼ 1900m) to the western one (∼ 100 m) were originates Rima Krieger. Comparable asymmetry in the rim height was also detected between the northern and southern rims of Van Biesbroeck crater. A sudden slope decrease referable to landslide deposits was identified in the Krieger north-western wall. The complex floor configuration is characterized by concentric linear features, hummocks, and large mounds (isolated or in clusters) ranging from 1 to 4 km in diameter and 30 to 400 m in height, with slopes between 20° and 40° (Collu et al., 2021).

applied to a spectral library of endmember spectra. The spectral library was constructed through two complementary approaches: endmember spectra were initially extracted from regions of interest identified based on the false-color composite and subsequently refined using the ENVI Pixel Purity Index (PPI) algorithm (Boardman, 1993; Boardman et al., 1995) to ensure spectral purity. Different maximum angle thresholds (ranging from 0.02 to 0.1 radians) were applied to each endmember spectrum, with more restrictive thresholds assigned to spectrally pure endmembers to account for variability in spectral signal. A similar approach using SAM and PPI applied to map the planetary surfaces was used by other authors, such as Serventi et al. (2021) on Mars and Carli et al. (2025) on the Moon.

Each spectrum in the library was individually analyzed to characterize its mineralogical affinity, considering continuum slope, band center position, band depth, band width, and band asymmetry (Cloutis & Gaffey, 1991; Horgan et al., 2014; Singer, 1981). Spectral band parameters were extracted using the IDL DISPEC software (Hecker et al., 2019), which applies a local continuum removal within user-defined wavelength intervals and calculates the shape parameters of individual absorption features. Three different interval configurations were adopted depending on the spectral characteristics of each unit. For spectra with two well-resolved absorption bands, Band I (adsorption feature near 1 μm) and Band II (adsorption feature near 2 μm) were analyzed separately over the intervals 730–1209 and 1578–2616 nm, respectively. For spectra showing a broad Band I absorption extending to longer wavelengths, the Band I interval was extended to 730–1578 nm,

**Table 1.** Detailed description of data utilized for photogeological observations, geomorphological and compositional analysis of the study area.

| Sensor | Mission | Product | Spatial resolution | Data used | Pre-processing |
|---|---|---|---|---|---|
| Narrow Angle Cameras (NACs) | Lunar Reconnaissance Orbiter (LRO) – NASA | CDRNAC 8-bit panchromatic | ~ 0.5 m/pixel | 40 calibrated images (sun incidence angles range from 0° to 80°) | Image co-registration with the LRO WAC imagery and SLDEM2015 |
| Moon Mineralogy Mapper (M3) | Chandrayaan-1 – ISRO | REFIMG photometrically calibrated reflectance data (430–3000 nm) | ~ 140 m/pixel | M3G20090209T033051_V01_RFL | Image co-registration with the LRO WAC imagery and SLDEM2015, spectral subsetting, and noise reduction were carried out using the Maximum Noise Fraction (MNF) method. |
| Lunar Orbiter Laser Altimeter (LOLA) and SELENE Terrain Camera (TC) | Lunar Reconnaissance Orbiter (LRO) – NASA Kaguya – JAXA | SLDEM2015 | 512 pixels per degree (~60 m at the equator), vertical accuracy of ~3–4 m. | sldem2015_512_00n_30n_315_360 sldem2015_512_00n_30n_270_315 | |

with Band II retained at 1578–2616 nm. For spectra exhibiting a poorly resolved or additional absorption feature between the two main bands, the intervals 730–1209 and 1778–2616 nm were used, to avoid including the intermediate feature in either band analysis (spectral units B2 and B3).

The integration of datasets with different spatial resolutions (NAC ~0.5 m/pixel, M3 ~60 m/pixel, SLDEM2015 ~140 m/pixel) was performed within a GIS environment, with all data co-registered to a common lunar coordinate system. High-resolution NAC imagery was used to define geomorphological unit boundaries, while M3 data provided compositional constraints at a broader scale. Where possible, compositional boundaries were refined using NAC imagery, particularly along crater walls and in areas where morphological and spectral variations showed spatial correspondence.

It should be noted that hyperspectral data are used here as compositional indicators to support the discrimination and interpretation of geomorphological units, rather than for quantitative mineralogical modeling. The analysis is therefore qualitative to semi-quantitative, focusing on relative variations in spectral properties rather than absolute mineral abundances.

The $M^3$ spectral analysis of the Krieger crater region reveals compositional variability consistent with a mixed assemblage of mare basaltic and pre-mare crustal materials. The false-color composite (Figure 3b) provides a first-order overview of this variability. Yellow hues characterize the mare basalt units, consistent with pyroxene-bearing compositions with strong absorptions at both 1 and 2 μm. Redder tones in the northern basaltic units suggest a relatively stronger Band I absorption, possibly reflecting increased olivine contribution or fresher mafic exposures. Bluish tones, reflecting high reflectance at 1.58 μm with weak mafic absorptions, occur in the ejecta south of Krieger, in the massif to the northwest, and in localized areas of the crater floor, consistent with feldspar-rich or highland-like compositions (Sarikaya et al., 2022). A purple signature along the northern rim of Van Biesbroeck crater is suggestive of an olivine-bearing composition associated with a high-albedo component.

A total of 18 representative spectra were extracted from the study area (Figure 3d–e) and analyzed through absorption band parameter extraction. All spectra exhibit two absorption bands near 1 and 2 μm, consistent with pyroxene-bearing assemblages, with band depths generally higher in fresh crater wall exposures and progressively attenuated in more mature surface units (Pieters et al., 2000).

The Band Area Ratio (BAR = Band II area/Band I area), plotted against Band I center position (Figure 3g), allows a first-order compositional grouping following Gaffey et al. (2002). Ten spectra show BAR > 1.5, consistent with pyroxene-dominated compositions. Three spectra (VW3, VW4, and VE3) show BAR < 0.30, Band I centers between 1.05 and 1.07 μm, and high positive Band I asymmetry (0.16–0.23), consistent with an increased olivine contribution to the spectral mixture (Horgan et al., 2014; Sunshine & Pieters, 1998). The remaining spectra show intermediate BAR values, suggesting variable pyroxene–olivine mixtures.

In the Band I vs. Band II center diagram (Figure 3f), most spectra plot within the low-Ca clinopyroxene field, consistent with pigeonite affinities. Spectrum VW1 plots within the orthopyroxene field, consistent with a low-Ca, Mg-rich pyroxene composition (Adams, 1974; Cloutis & Gaffey, 1991), while spectra B2, B3, and VE2 shift toward higher-Ca clinopyroxene compositions. Spectrum KCP, extracted from a

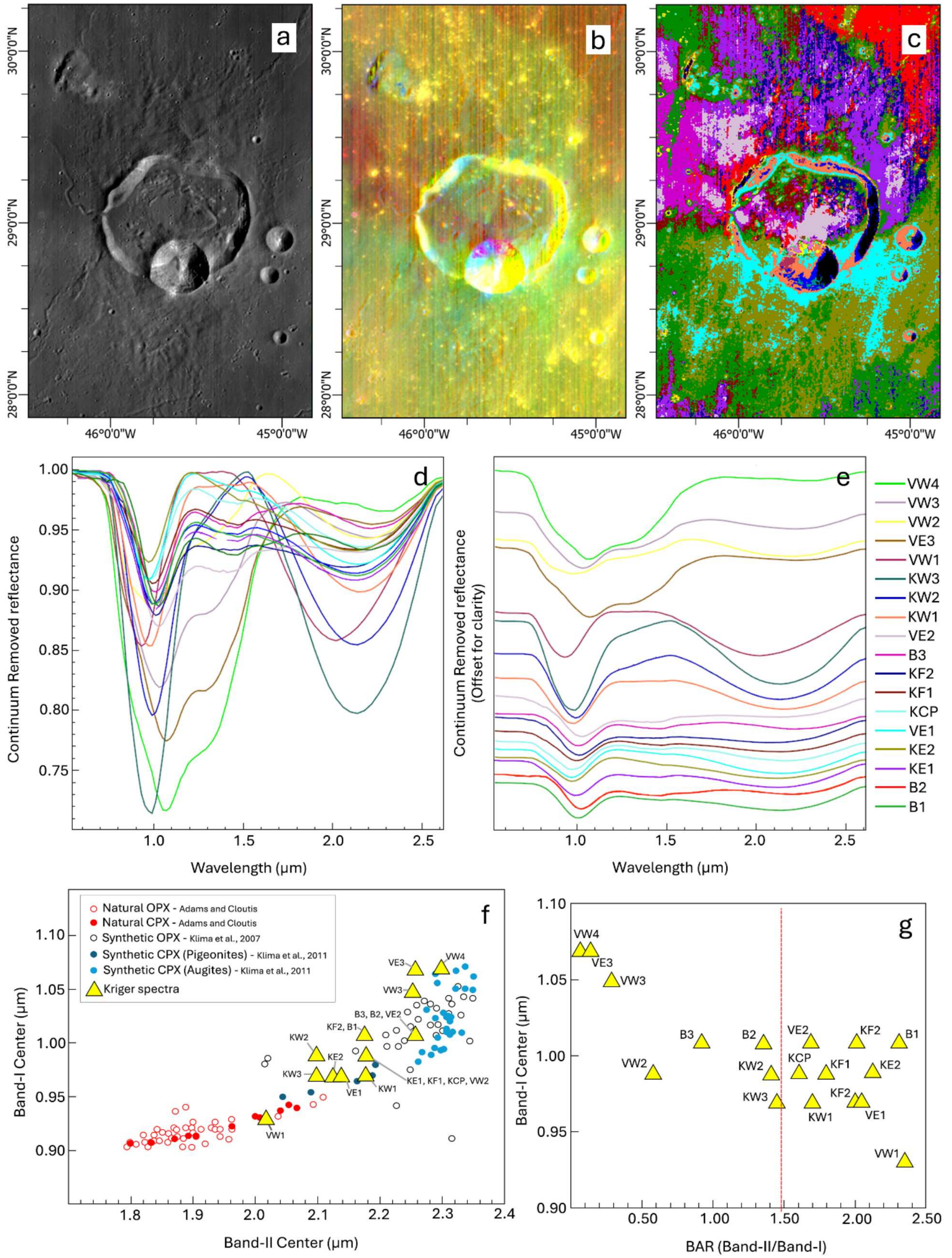


**Figure 3.** $M^3$-based spectral analysis of the Krieger crater region. (a) $M^3$ reflectance image. (b) False-color composite (R = 1 μm integrated band depth; G = 2 μm integrated band depth; B = reflectance at 1.58 μm). (c) SAM compositional map. (d) Continuum-removed reflectance spectra of the 18 extracted endmembers. (e) Continuum-removed reflectance spectra offset for clarity, with unit labels. (f) Band I vs. Band II center diagram with reference fields from Adams (1974) as modified by Cloutis and Gaffey (1991) and synthetic pyroxene data from Klima et al. (2007, 2011). (g) BAR vs. Band I center diagram; dashed red line indicates the pyroxene threshold (BAR = 1.5) after Gaffey et al. (2002).

topographic high in the crater interior, shows the most strongly negative Band I asymmetry (−0.21) and no detectable olivine contribution, with a low-Ca pyroxene affinity.

Based on these results, and integrating the morphostructural and photogeological interpretation, the study area was subdivided into 20 geomorphological units grouped into Highland, Mare, and Crater-related deposits. The classification follows a hierarchical scheme, though the criteria applied at each level may vary depending on the unit considered. At the first level, the surface was subdivided into macro-units based on morphological criteria, identifying the main geological domains: ejecta deposits, crater wall, crater floor, mare, and highland. These units are further differentiated based on age: the 'K' codification refers to the Imbrian crater Krieger, whereas the 'E' codification is used for Eratosthenian craters (Van Biesbroeck, Rocco, and Ruth). At the second level, each macro-unit was further subdivided into numbered units based on either spectral characteristic, morphological features, or a combination of both, depending on the dominant discriminating factor observed for each specific unit. At the third level, sub-units (suffix a and b) were defined exclusively based on surface texture, distinguishing smooth and planar surfaces (suffix a) from hummocky and irregular surfaces (suffix b), at equal spectral composition.

From a morphological point of view, the units were distinguished based on surface texture, roughness, and albedo variations as observed in LROC NAC images. Spectral criteria derived from the M3 hyperspectral data, including the Spectral Units defined in the previous section, were also used to further differentiate units that appeared morphologically similar but showed distinct spectral signatures.

Detailed descriptions of the units are provided below and summarized in the legend of the Main Map.

### 2.1. Highland units

The Highland Massif (**Hm**) unit consists of a large block rising above the adjacent low terrain to the northwest of Krieger crater. Mapped as pre-Imbrian material (Wilhelms & McCauley, 1971; Zisk et al., 1977), it is spectrally characterized by high reflectance at 1.58 μm and weak mafic absorptions, consistent with highland-like compositions.

### 2.2. Mare units

Mare Units are characterized by basalt-like compositions and smooth, planar surfaces, typical of mare basaltic lava materials. PL7 Unit and L4 Unit, identified previously by Zhang et al. (2014), originated from two different effusive episodes, both presenting spectral signatures with weak absorption features, which suggest a rich-glass soil nature, indicating a high degree of space-weathering maturity. As reported in Zhang et al. (2014), **PL7** basalts (spectrum B1) are the most ancient materials in the region, with low-Ti and low-olivine content, and a pyroxene-dominant composition, while **L4** basalts (spectrum B2) show a higher content in TiO and olivine, and a lower density of impact craters. These characteristics are typical of late-Imbrian volcanism (Zhang et al., 2014).

The Krieger Basalts unit (**KB**) consists of smooth to hummocky basaltic deposits extending beyond the breached western rim of Krieger crater, likely emplaced through the rim breach via lava outflow from the crater interior, a process consistent with the sinuous morphology of Rima Krieger, interpreted as a lava channel formed by effusion through the western rim low point (Hurwitz et al., 2012). The unit shares spectral characteristics with the Kf3 geomorphological unit, with Band II centers near 2257 nm, shifted toward longer wavelengths relative to the majority of the analyzed spectra, suggesting a higher-Ca pyroxene affinity compared to the dominant basaltic units of the study area.

### 2.3. Craters' Ejecta units

Crater Ejecta Units represent deposits excavated by impacts and emplaced outside the crater rim. Ejecta deposits related to the Krieger impact are divided into two units: Krieger Ejecta 1 (**Ke1**) in the northern part and Krieger Ejecta 2 (**Ke2**) in the southern part and near the northern rim. Ke1 deposits show a rougher surface morphology and appear thicker than the southern Ke2 deposits, as observed in the SLDEM2015-derived topography (Figure 2), possibly reflecting variations in pre-existing target morphology and/or regional structural control associated with nearby wrinkle ridges (Collu et al., 2021). Spectrally, Ke1 and Ke2 are consistent with a pyroxene-dominated composition (spectra KE1 and KE2), analogous to the surrounding mare basalt units. Near the northern rim, Ke2 displays melt features, flow channels, and ejecta blocks ranging from 10 to 140 m in diameter.

Ejecta deposits from the Eratosthenian craters Van Biesbroeck, Rocco, and Ruth are differentiated into two units. **Ece1** displays high reflectance at 1.58 μm and weak mafic absorptions (spectrum VE1), analogous to the spectral characteristics described for the Hm and Ke2 units. **Ece2** shows intermediate BAR values and Band II centered near 2257 nm (spectrum VE2), consistent with a pyroxene–olivine mixture with higher-Ca pyroxene affinity. Small melt-coating features near the crater rim exhibit the most olivine-bearing signature in the dataset (spectrum VW4), with Band I at 1069 nm, BAR = 0.07, and very weak Band II absorption (Horgan et al., 2014; Sunshine & Pieters, 1998).

### 2.4. Crater Wall units

In contrast to the surrounding mare and highland units, Crater Wall units display significantly deeper absorption bands, with Band I depths exceeding 1 and reaching up to 2.80 (spectra KW1, KW2, KW3, VW1), consistent with the exposure of relatively unweathered material along steep slopes, where mass wasting, scarps, melt coating features, and boulder deposits (Figure 4) limit the accumulation of mature regolith (Pieters et al., 2000).

In the Krieger walls, 3 different crater wall units were identified: Krieger Wall 1 (**Kw1**), Krieger Wall 2 (**Kw2**), and Krieger Landslide (**KL**). The Kw1 unit, extending along the upper and lower walls, displays mid-low surface roughness with relatively low slopes, and shows boulder rolling features, block deposits, and melt sheet features near the crater rim. Spectrally, it is consistent with a pyroxene-dominated composition (spectrum KW1, BAR = 1.70). The Kw2 unit presents steeper and rougher surfaces covered by thin melt veneers and coarse debris flows, with spectral characteristics suggesting a possible olivine contribution (spectrum KW2, BAR = 1.41, Band I asymmetry = + 0.19) (Figure 5). The Krieger Landslide unit (KL) is located along the north-western wall of Krieger crater and displays a morphology typical of mass wasting processes, characterized by a well-defined detachment scarp in the upper wall and a corresponding accumulation deposit at its base. Compared to the other crater wall units, KL shows significantly lower slopes and smoother surfaces. Spectrally, this unit is compositionally similar to the crater floor units.

Eratosthenian crater walls of Van Biesbroeck, Rocco, and Ruth show the freshest materials. Eratosthenian Crater Wall 1 Unit includes the subunits **Ecw1a** and **Ecw1b**, identical in composition and morphology to the Kw1 and Kw2 units respectively, while Eratosthenian Crater Wall 2 Unit (Ecw2) and Eratosthenian Crater Wall 3 Unit (Ecw3) show a unique composition. The Ecw2 unit (spectrum VW1) is characterized by steep and highly rough surfaces with boulder deposits, possibly suggesting an impact melt breccia's nature. Spectrally, it displays Band I centered at 930 nm and Band II at 2018 nm, consistent with a low-Ca, Mg-rich pyroxene composition, analogous to orthopyroxene (Adams, 1974; Cloutis & Gaffey, 1991). Ecw3 is characterized by smooth melt coating features interrupted by high rough surfaces exposing fresh materials, frequent slope failures, slumps, and mass wasting features. The spectral characteristics of this unit, as described in the Results section, indicate pyroxene–olivine mixtures of variable composition, ranging from pyroxene-bearing assemblages with minor olivine contribution to nearly olivine-dominant compositions (spectra VE3, VW2, VW3, VW4).

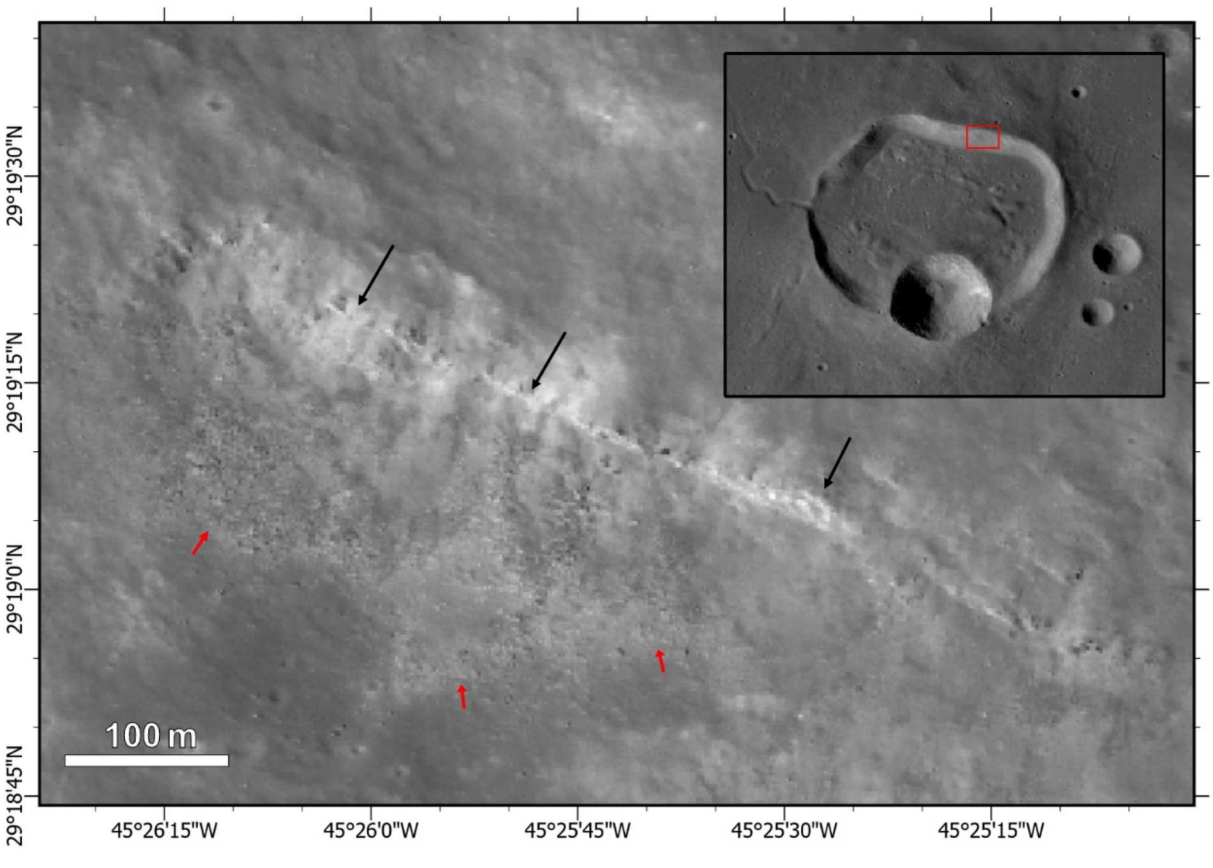


**Figure 4.** The NAC image of the north-eastern wall of Krieger crater shows scarps (black arrows) and mass wasting morphologies (red arrows).

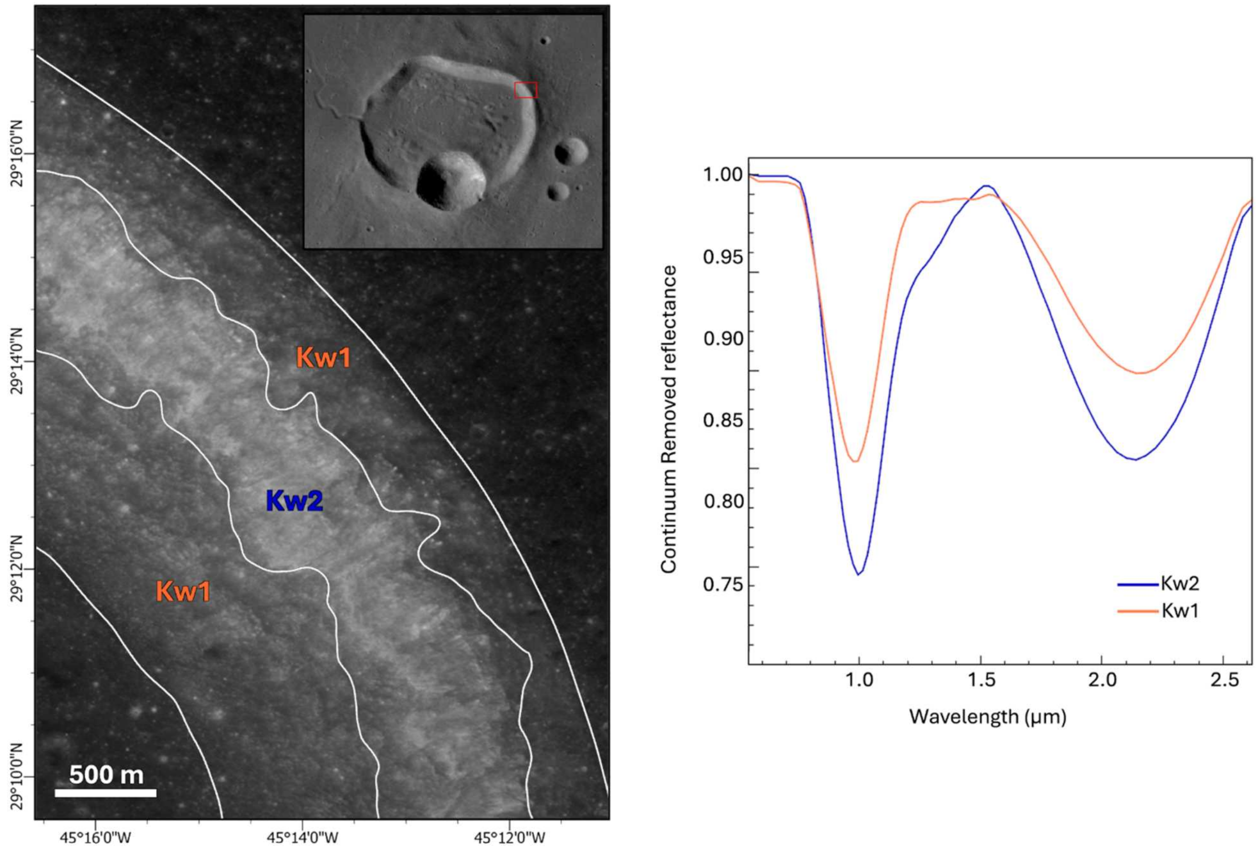


**Figure 5.** NAC image of the north-eastern wall of Krieger crater showing the albedo variation between the Kw1 and Kw2 units, related to differences in surface texture and composition. The corresponding continuum-removed $M^3$ spectra show pyroxene-dominated compositions for both units, with Band I centered near 0.97–0.99 µm and Band II near 2.10 µm. KW2 displays significantly deeper absorption features than KW1 and a slightly broader and more positively asymmetric Band I (asymmetry = + 0.19), suggesting a minor olivine contribution to the spectral mixture (Sunshine & Pieters, 1998).

### 2.5. Craters Floor units

Craters Floor Units represent the most interesting deposits and morphologies of the study area, because they provide many indications about post-impact processes. Van Biesbroeck, Rocco, and Ruth are simple craters, thus presenting a single floor unit, named Eratosthenian Crater Floor (**Ecf**), characterized by hummocky surfaces and mass wasting deposits with frequent blocks (Figure 6). This floor configuration is interpreted as a primary crater-related morphology resulting from impact excavation, ejecta fallback, and localized wall collapse during the crater formation stage. The Ecf unit shows a composition similar to Ece1 unit.

On the contrary, Krieger floor reveals a complex configuration, with the presence of concentric linear features consisting of subtle alignments of small mounds and shallow depressions arranged concentrically with respect to the crater center. Due to their diffuse and discontinuous nature, they do not constitute discrete mappable structures and have therefore not been included as individual units in the geomorphological map. Hummocks and large mounds (isolated or in clusters) have similar spectral characteristics of Ke2 and PL7 units, included in the Krieger Mounds Unit (**Km**), whereas a possible central peak, incorporated in the Krieger Central Peak Unit (**Kcp**), is characterized by a rougher surface texture and a higher crater density compared with the other reliefs. The spectral characteristics (KCP spectrum, pyroxene-dominated composition with no detectable olivine contribution and low-Ca pyroxene affinity) may suggest the exposure of pre-mare crustal material, although an origin related to floor uplift associated with sub-floor magmatic intrusion cannot be excluded on spectral grounds alone (Jozwiak et al., 2012, 2015; Schultz, 1976).

Krieger Floor 4 Unit (**Kf4**), located in the central part of the crater, surrounds the Kcp Unit and shows pyroxenes-dominant composition (spectrum KF1, BAR = 1.80), and it is characterized by smooth and plane morphology, presenting a higher crater density compared to hummocky crater floor units. Additional Krieger floor units are subdivided into sub-units exclusively based on the surface morphology: '-a' suffix stands for smooth and plane surfaces, while '-b' suffix represents hummocky and irregular surfaces. Krieger Floor 1 Unit (**Kf1**) extends in the northern part of the Krieger floor, and it shows a

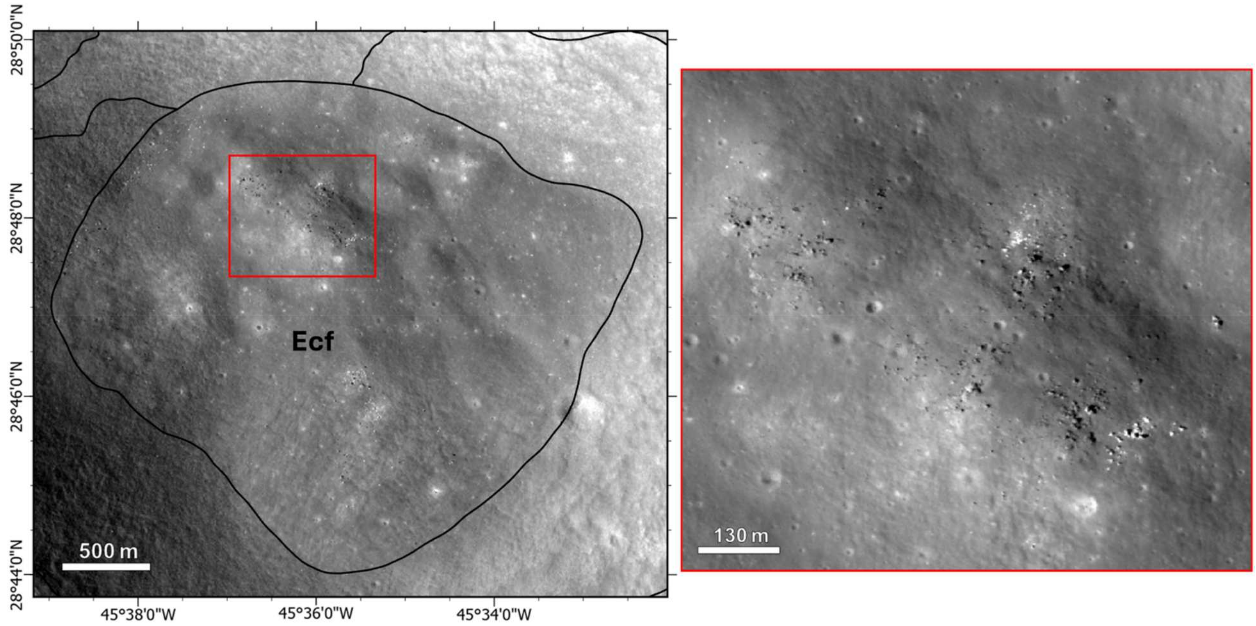


**Figure 6.** LROC NAC image of Van Biesbroeck's floor, characterized by a hummocky surface and mass wasting deposits.

spectral signature similar to the Ke2 Unit. Krieger Floor 2 (**Kf2a** and **Kf2b**) displays a smoother surface texture compared to Kf1 and a spectrally analogous pyroxene-dominated composition (spectrum KF2, BAR = 2.01), with Band I and Band II centered at 1009 and 2177 nm, respectively.

## 3. Discussion

Spectral and geomorphological analysis of the Krieger crater region reveals various landforms and surface mineralogical compositions, which led to the identification of 20 geomorphological units. The spatial distribution of mineral compositions, along with the unique morphological configuration of the Krieger crater floor, provides insights into the geodynamic processes that affected the study area.

According to Hiesinger et al. (2003) and Zhang et al. (2014), the most ancient unit in the region is the PL7 Unit, a basaltic material characterized by low titanium and low olivine content, emplaced during the Imbrian Period (Hiesinger et al., 2003). Following this stage, the formation of Krieger crater is consistent with an oblique impact scenario, as suggested by the asymmetric ejecta distribution, rim height variations, and the presence of a displaced central peak. In addition, regional structural inheritance may have contributed to the observed rim morphology.

The geomorphological units related to this stage, immediately following the impact, include the ejecta deposits (Ke1, Ke2), the Krieger Wall units (Kw1, Kw2), and the Krieger Floor units, including the central peak (Kcp) and the units with higher crater density (Kf1a and Kf4), which likely represent early impact-related materials, including possible impact melt products.

The complex floor configuration and the presence of pyroxene–olivine mixed compositions in units Kf2 and Kf3 indicate intense post-impact modification processes, typical of floor-fractured craters (Jozwiak et al., 2012; Schultz, 1976). Within this framework, these features may reflect floor uplift and magmatic intrusion beneath the crater, as proposed for similar lunar FFC structures. Such processes could have led to partial resurfacing of the crater floor, including the emplacement of Kf2a and Kf3a units, and the development of concentric fractures, hummocky terrains, and mound-like structures (Km, Kf1b, Kf2b, and Kf3b).

The similarity between the spectral response of Kf3 and Krieger Basalts (KB) suggests a possible genetic or compositional link between these units. This observation is consistent with the broader evolutionary framework of floor-fractured craters, in which subsurface magmatic activity may facilitate localized volcanic resurfacing and, in some cases, outward lava emplacement. In this context, the relationship between KB and L4-like basalts may indicate temporally or compositionally related volcanic episodes, although absolute synchrony cannot be demonstrated with the available dataset.

During the Eratosthenian period, subsequent impact events such as Van Biesbroeck excavated portions of the crater floor, exposing deeper materials, including olivine-bearing materials observed in its ejecta and wall exposures. The compositional variability observed in surrounding ejecta deposits may also reflect regional mixing processes and contributions from nearby large impact events, including Aristarchus.

## 4. Conclusions

Overall, this study on Krieger crater contributes to the existing literature by providing an integrated geomorphological and spectral framework that helps to better understand the complexity of floor-fractured crater (FFC) systems and their surface expression, while acknowledging the inherent limitations of the present methodology, which is intended as a qualitative to semi-quantitative approach, aimed at identifying compositional trends and relative spectral variations rather than deriving precise mineral abundances.

Future work should address these limitations by integrating quantitative spectral unmixing techniques, higher-resolution spectral datasets, and statistical validation approaches to better constrain surface composition. Furthermore, crater counting methodologies could provide additional temporal constraints on the evolution of the different geomorphological units, improving the reconstruction of the crater's geological history.

## Software

Hyperspectral data from the M3 sensor were processed and analyzed using ENVI (version 3.6). This included full pre-processing of the M3 reflectance data, selection of areas of interest, creation of a spectral library, and classification of surface compositional units using the Spectral Angle Mapper (SAM) algorithm. Spectral band parameters were extracted using the IDL DISPEC software. Geomorphological mapping and spatial analyses were performed using ArcGIS Pro (version 3.6), which was employed for data integration, georeferencing, visualization, generation of topographic sections and compilation of the high-resolution geomorphological map.

## Acknowledgments

This research was developed within the framework of the Moon Mapping Project, a scientific cooperation initiative established between Italian and Chinese institutions to promote joint lunar mapping and training of new researchers on remotely sensed lunar data. The project involved collaboration among Italian universities and research centers and Chinese universities and research institutions, coordinated by the Italian Space Agency (ASI) and the Center of Space Exploration under the Ministry of Education, P.R. China. The authors acknowledge the support and collaboration fostered through this international project, which provided a valuable context for the development of the geomorphological analysis presented here.

## Author contributions

CRediT: **Claudia Collu:** Conceptualization, Data curation, Formal analysis, Investigation, Methodology, Visualization, Writing – original draft; **Marco Casu:** Data curation, Software, Supervision, Validation, Visualization, Writing – review & editing; **Francesco Dessì:** Conceptualization, Data curation, Software, Supervision, Validation, Writing – review & editing; **Maria Teresa Melis:** Conceptualization, Funding acquisition, Project administration, Resources, Validation, Writing – review & editing.

## Disclosure statement

No potential conflict of interest was reported by the author(s).

## Data availability statement

All data used in this study are publicly available from the respective missions and sources, as cited in the manuscript. No additional datasets were generated or deposited.

## ORCID

*Maria Teresa Melis* http://orcid.org/0000-0003-0970-1244

## References

Adams, J. B. (1974). Visible and near-infrared diffuse reflectance spectra of pyroxenes as applied to remote sensing of solid objects in the Solar System. *Journal of Geophysical Research*, *79*(32), 4829–4836. https://doi.org/10.1029/JB079i032p04829

Boardman, J. W. (1993). Automating spectral unmixing of AVIRIS data using convex geometry concepts. *In: Summaries of the 4th Annual JPL Airborne Geoscience Workshop, JPL Pub. 93-26, AVIRIS Workshop, 1* (pp. 11–14).

Boardman, J. W., Kruse, F. A., & Green, R. O. (1995). Mapping target signatures via partial unmixing of AVIRIS data. In *Summaries of the 5th Annual JPL Airborne Earth Science Workshop, Pasadena, CA* (pp. 23–26).

Carli, C., Giacomini, L., Serventi, G., & Sgavetti, M. (2025). Geological Map of the Proclus Crater: A study case to integrate composition and Morpho-Stratigraphic mapping on the Moon. *Remote Sensing*, *17*(23), 3786. https://doi.org/10.3390/rs17233786

Cloutis, E. A., & Gaffey, M. J. (1991). Pyroxene spectroscopy revisited: Spectral-compositional correlations and relationship to geothermometry. *Journal of Geophysical Research: Planets*, *96*(E5), 22809–22826. https://doi.org/10.1029/91JE02512

Cloutis, E. A., Gaffey, M. J., Jackowski, T. L., & Reed, K. L. (1986). Calibrations of phase abundance, composition, and particle size distribution for olivine-orthopyroxene mixtures from reflectance spectra. *Journal of Geophysical Research: Solid Earth*, *91*(B11), 11641–11653. https://doi.org/10.1029/JB091iB11p11641

Collu, C., Podda, S., & Melis, M. T. (2021). Morphological and compositional investigation of Krieger Crater (Moon). In *AIT Conference* 2021, Poster session.

Gaffey, M. J., Cloutis, E. A., Kelley, M. S., & Reed, K. L. (2002). Mineralogy of asteroids. In W. F. Bottke, A. Cellino, P. Paolicchi, & R. P. Binzel (Eds.), *Asteroids III* (pp. 183–204). University of Arizona Press.

Hecker, C., van Ruitenbeek, F. J. A., van der Werff, H. M. A., Bakker, W. H., Hewson, R. D., & van der Meer, F. D. (2019). Spectral absorption feature analysis for finding ore: A tutorial on using the method in geological remote sensing. *IEEE Geoscience and Remote Sensing Magazine*, *7*(2), 51–71. https://doi.org/10.1109/MGRS.2019.2899193

Hiesinger, H., Head, J. W., Wolf, U., Jaumann, R., & Neukum, G. (2003). Ages and stratigraphy of mare basalts in Oceanus Procellarum, Mare Nubium, Mare Cognitum, and Mare Insularum. *Journal of Geophysical Research: Planets*, *108*(E7), 1–27. https://doi.org/10.1029/2002JE001985

Horgan, B. H. N., Cloutis, E. A., Mann, P., & Bell, J. F. (2014). Near-infrared spectra of ferrous mineral mixtures and methods for their identification in planetary surface spectra. *Icarus*, *234*, 132–154. https://doi.org/10.1016/j.icarus.2014.02.031

Hurwitz, D. M., Head, J. W., Wilson, L., & Hiesinger, H. (2012). Origin of lunar sinuous rilles: Modeling effects of gravity, surface slope, and lava composition on erosion rates during the formation of Rima Prinz. *Journal of Geophysical Research: Planets*, *117*(E12), E00H–14. https://doi.org/10.1029/2011JE004000

Jozwiak, L. M., Head, J. W., & Wilson, L. (2015). Lunar floor-fractured craters as magmatic intrusions: Geometry, modes of emplacement, associated tectonic and volcanic features, and implications for gravity anomalies. *Icarus*, *248*, 424–447. https://doi.org/10.1016/j.icarus.2014.10.052

Jozwiak, L. M., Head, J. W., Zuber, M. T., Smith, D. E., & Neumann, G. A. (2012). Lunar floor-fractured craters: Classification, distribution, origin and implications for magmatism and shallow crustal structure. *Journal of Geophysical Research: Planets*, *117*(E11), E11005. https://doi.org/10.1029/2012JE004134

Kenkmann, T., Poelchau, M. H., & Wulf, G. (2014). Structural geology of impact craters. *Journal of Structural Geology*, *62*, 156–182. https://doi.org/10.1016/j.jsg.2014.01.015

Klima, R. L., Dyar, M. D., & Pieters, C. M. (2011). Near-infrared spectra of clinopyroxenes: Effects of calcium content and crystal structure. *Meteoritics & Planetary Science*, *46*(3), 379–395. https://doi.org/10.1111/j.1945-5100.2010.01158.x

Klima, R. L., Pieters, C. M., & Dyar, M. D. (2007). Spectroscopy of synthetic Mg-Fe-Ca pyroxenes I: Spin-allowed and spin-forbidden crystal field bands in the visible and near-infrared. *Meteoritics & Planetary Science*, *42*(2), 235–253. https://doi.org/10.1111/j.1945-5100.2007.tb00229.x

Kruse, F. A., Lefkoff, A. B., Boardman, J. W., Heidebrecht, K. B., Shapiro, A. T., Barloon, P. J., & Goetz, A. F. H. (1993). The spectral image processing system (SIPS) – Interactive visualization and analysis of imaging spectrometer data. *Remote Sensing of Environment*, *44*(2-3), 145–163. https://doi.org/10.1016/0034-4257(93)90013-N

Pieters, C. M., Taylor, L. A., Noble, S. K., Keller, L. P., Hapke, B., Morris, R. V., Allen, C. C., McKay, D. S., & Wentworth, S. (2000). Space weathering on airless bodies: Resolving a mystery with lunar samples. *Meteoritics & Planetary Science*, *35*(5), 1101–1107. https://doi.org/10.1111/j.1945-5100.2000.tb01496.x

Podda, S., Melis, M. T., Collu, C., Demurtas, V., Perseu, F. O., Brunetti, M. T., & Scaioni, M. (2020). New morphometric data of lunar sinuous rilles. *IEEE Journal of Selected Topics in Applied Earth Observations and Remote Sensing*, *13*, 3304–3316. https://doi.org/10.1109/JSTARS.2020.3003080

Sarikaya, M., Rajesh, H. M., & Vijayan, S. (2022). An investigation on the morphological and mineralogical characteristics of Posidonius floor fractured lunar impact crater using lunar remote sensing data. *Remote Sensing*, *14*(4), 814. https://doi.org/10.3390/rs14040814

Schultz, P. H. (1976). Floor-fractured lunar craters. *The Moon*, *15*(3-4), 241–273. https://doi.org/10.1007/BF00562240

Serventi, G., Carli, C., Altieri, F., & Sgavetti, M. (2021). Spectral classification and MGM-based mineralogical characterization of hydrated phases: "The Nili Fossae case", Mars. *Planetary and Space Science*, *209*, 105361. https://doi.org/10.1016/j.pss.2021.105361

Singer, R. B. (1981). Near-infrared spectral reflectance of mineral mixtures: Systematic combinations of pyroxenes, olivine, and iron oxides. *Journal of Geophysical Research: Solid Earth*, *86*(B9), 7967–7982. https://doi.org/10.1029/JB086iB09p07967

Sunshine, J. M., & Pieters, C. M. (1998). Determining the composition of olivine from reflectance spectroscopy. *Journal of Geophysical Research: Planets*, *103*(E6), 13675–13688. https://doi.org/10.1029/98JE01217

Wilhelms, D. E., & McCauley, J. F. (1971). *Geologic Map of the Near Side of the Moon*, USGS Miscellaneous Investigations Series Map I-703, scale 1:5,000,000. U.S. Geological Survey.

Zhang, F., Zou, Y. L., Zheng, Y. C., Fu, X. H., & Zhu, Y. C. (2014). Lunar mare basalts in the aristarchus region: Implications for the stratigraphic sequence from clementine UVVIS data. *Icarus*, *227*, 132–151. https://doi.org/10.1016/j.icarus.2013.09.011

Zisk, S. H., Hodges, C. A., Moore, H. J., Shorthill, R. W., Thompson, T. W., Whitaker, E. A., & Wilhelms, D. E. (1977). The Aristarchus-Harbinger region of the moon: Surface geology and history from recent remote-sensing observations. *The Moon*, *17*(1), 59–99. https://doi.org/10.1007/BF00566853